PAPER

Study on the properties of Pb–Co$_3$O$_4$–PbO$_2$ composite inert anodes prepared by vacuum hot pressing technique

Jingshi Zhang, [ID] [ab] Ruidong Xu, *[ab] Bohao Yu, [ID] [a] Yunlong He, [a] Yiyang Li [a] and Ziyang Qin [a]

Pb–PbO$_2$, Pb–Co$_3$O$_4$ and Pb–Co$_3$O$_4$–PbO$_2$ composite inert anodes were prepared by vacuum hot pressing technique from the mixtures of lead powders, Co$_3$O$_4$ and PbO$_2$ particles in a fixed mould. The influences of heating temperatures and particles doping on the properties of the composite inert anodes were researched. The surface microstructures, phase structures and electrochemical properties were measured by X-ray diffraction (XRD), scanning electronic microscopy (SEM), energy dispersive spectrometer (EDS), anodic polarization curves (AP), cyclic voltammetry curves (CV), Tafel polarization curves and electrochemical impedance spectroscopy (EIS). The results showed that the uniform distributions of Co$_3$O$_4$ and PbO$_2$ as the second phase particles in the composite inert anodes have been obtained by the vacuum hot pressing technique. The lead powders were melted and formed a uniform and compact matrix, in which the morphologies and properties of Co$_3$O$_4$ and PbO$_2$ particles were kept. The electrochemical property and corrosion resistance of the composite inert anodes in a zinc electrowinning simulation solution were improved with the rise of heating temperatures during the vacuum hot pressing, and those were also enhanced by the doping of Co$_3$O$_4$ and PbO$_2$ particles. This method solved the problems of the lower dispersion uniformity of the composite inert anodes prepared by composite electrodeposition or traditional casting technique.

1. Introduction

Composite inert anodes used in zinc electrowinning have been studied widely for many years. The direction of reaction, kinetics of electrode course, structure patterns of the electrolytic cell and electric energy consumption are not only related to the electrolyte characteristics, but also related to the performance of anode materials in zinc electrowinning.[1,2] The Pb–Ag (0.75–1.0 wt%) and Pb–Ag (0.2–0.3 wt%)–Ca (0.06–0.1 wt%) alloy anodes are widely used in zinc electrowinning industry in view of their good stability and high corrosion resistance in acid solution. However, they have some shortcomings such as poor conductivity, high overpotential of oxygen evolution, and dissatisfactory mechanical performance.[3–5] In order to solve shortcomings, precious metal or other metal (*i.e.* silver, calcium and thallium in lead alloy) has added in inert anodes by R. H. Newnham.[6] Active particles such as tungsten carbide and cobalt oxide have been doped in Al/Pb/α-PbO$_2$ inert anodes by S. He *et al.*[7] The Al/Pb–Ag alloy anodes were studied by Y. Zhang *et al.* which were obtained by electrodeposition on aluminum matrix.[8]

In order to solve the above problems, there are two main optimization routes by researchers.[9–14] (i) The electrocatalytic activity, corrosion resistance and mechanical properties are improved by binary alloy and multi-component alloy base on Pb substrate such as Pb–Ag, Pb–Sn, Pb–Ca, Pb–Ba, Pb–Cd, Pb–Ag–Ca, Pb–Ag–Ti and Pb–Ag–Sn.[15–18] But there are still some defects such as high energy consumption and short service life. (ii) The electrocatalytic activity, corrosion resistance and mechanical properties are improved by the metal substrate film anodes such as MnO$_2$, PbO$_2$ and platinum group oxide prepared by composite electrodeposition and other methods, and Ti, Al, Pb and stainless steel can be used as main substrates. However, there are still some deficiencies of short service life and lower dispersion uniformity.[19]

Co$_3$O$_4$ particle as a metal oxide catalytic agent has extensive applications for catalyst to electrode.[20] It is widely used in the fields of super capacitor, ceramic and catalyst, and has shown excellent electrochemical properties such as electrocatalytic capacity, electrocatalytic activity of oxygen evolution.[21,22] In order to obtain Pb–Co$_3$O$_4$–PbO$_2$ composite inert anodes used in zinc electrowinning, the molten metal (traditional casting) method was used firstly, But Co$_3$O$_4$ and PbO$_2$ particles could not be wetted into molten lead, leading that the blending homogeneity of particles in the composite inert anodes could not controlled. The vacuum hot pressing method as a kind of

[a]*Faculty of Metallurgical and Energy Engineering, Kunming University of Science and Technology, Kunming 650093, China. E-mail: rdxupaper@aliyun.com*

[b]*State Key Laboratory of Complex Nonferrous Metal Resources Clean Utilization, Kunming 650093, China*

powder metallurgy process can be carried out under low-temperature condition, which reduces diffusion rates and controls the interface reaction kinetics.[23-25] It has been used to prepare diamond/Al, diamond/Si–Cu and Al–Cu–Fe composites.[26-28]

In this research, Pb–Co_3O_4–PbO_2 composite inert anodes were prepared by vacuum hot pressing technique from the mixtures of Pb powders, Co_3O_4 and PbO_2 particles in a fixed mould, which solved the problems of the failure and lower blending homogeneity of the composite inert anodes prepared by composite electrodeposition or traditional casting technique, and a better electrochemical property has been obtained in a zinc electrowinning simulation solution. During the vacuum hot pressing, the influences of the heating temperatures and particles doping on the preparation and properties of the composite inert anodes were investigated. The surface morphologies, phase structures and electrochemical properties of the composite inert anodes were measured by scanning electronic microscopy, X-ray diffractometer and electrochemical workstation.

2. Experimental

2.1 Preparation of the composite inert anodes

Lead powder (Pb, purity: 99.9%), cobalt oxide (Co_3O_4, purity: 99.9%) and lead dioxide (PbO_2, purity $\geq$ 97.0%) were used in the experiments. The molar ratio of Pb/PbO_2 or Pb/Co_3O_4 was 10 : 1, and that of Pb/PbO_2/Co_3O_4 was 10 : 1 : 1. Firstly, the mixtures of Pb, Co_3O_4 and PbO_2 powders were blended homogeneously by using agate mortar for 30 minutes. Then, the blended powders were placed into graphite mould with inner and outer diameters of 30 and 85 mm respectively in the vacuum hot press furnace. Thereafter, the furnace was vacuumized to 10^{-3} Pa, a pressure of 65 MPa and a heating rate of 10 °C min^{-1} were provided. The heating temperatures were controlled ranges of 260 °C to 340 °C, 260, 280, 300, 320, 340 °C respectively, and the heating time was controlled at 45 min. And then, furnace was begun to cool. When furnace temperature was cooled down to 80 °C, the air would be pumped in the furnace, and when furnace temperature was cooled down to 60 °C, the graphite mould would be brought out. Finally, Pb–PbO_2, Pb–Co_3O_4 and Pb–Co_3O_4–PbO_2 composite inert anodes were obtained by vacuum hot pressing method in ZT-30-16Y vacuum hot press furnace.

2.2 Measurements of the composite inert anodes

All electrochemical measurements in the zinc electrowinning simulated electrolyte were carried out by a PARATAT2273 electrochemical workstation with a standard three-electrode system. The composite inert anode was employed as the working electrode and its active area was 1 cm^2, the reference electrode was a saturated calomel electrode (SCE) and the counter electrode was a graphite electrode. The reference electrode and working electrode were linked by a Luggin capillary filled with agar and potassium chloride. In addition, the distance between the capillary and working electrode surface was about 2d (d is the diameter of capillary), and d was 0.5 mm.

The compositions of the zinc electrowinning simulated electrolyte solution were as follows: 50 g L^{-1} Zn^{2+} and 150 g L^{-1} H_2SO_4, the test temperature was controlled at 35 °C. Anodic polarization curves (AP), cyclic voltammetry curves (CV), Tafel polarization curves and electrochemical impedance spectroscopy (EIS) were obtained in the zinc electrowinning simulated electrolyte system. In addition, phase structures of the composite inert anodes were measured by D/Max-2200 X-ray diffractometer, the surface morphologies and the chemical compositions of the composite inert anodes were measured by VEGA3-SBH scanning electronic microscopy with UltroDry energy dispersive spectrometer.

3. Results and discussion

3.1 Anodic polarization curves of the composite inert anodes

Anodic polarization curves of Pb–Co_3O_4 composite inert anodes obtained at different heating temperatures were measured in the zinc electrowinning simulated solution, and the results were shown in Fig. 1. The inset is the Tafel lines ($\eta = a + b \lg i$) of the oxygen evolution reaction.[29-31] The kinetic parameters of Tafel linear fitting and oxygen evolution overpotentials of the composite inert anodes obtained at different heating temperatures were shown in Table 1.

As shown in Fig. 1 and Table 1, the oxygen evolution potentials or overpotentials decreased with the rise of heating temperatures from 260 °C to 340 °C, displaying that increasing heating temperature was favourable to the reduction of oxygen evolution potentials or overpotentials of the composite inert anodes in the zinc electrowinning simulated solution. The composite inert anodes obtained by the heating temperature of 340 °C possessed the lowest oxygen evolution overpotentials with 0.768, 0.792 and 0.817 V at the current densities of 400, 500 and 600 A m^{-2}, displaying that the electrocatalytic activity of Pb–Co_3O_4 composite inert anode was the best in the zinc electrowinning simulation solution.

Pb–Co_3O_4 composite inert anode obtained at 340 °C possessed the lowest oxygen evolution overpotentials and the
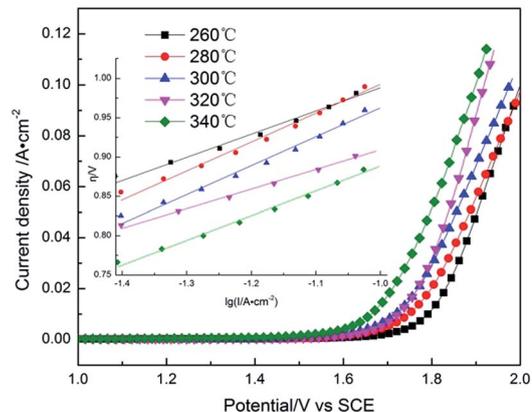

Fig. 1 Anodic polarization curves of Pb–Co_3O_4 composite inert anodes obtained at different heating temperatures (scanning rate: v = 5 mV s^{-1}).

Table 1 Oxygen evolution overpotential and kinetic parameters of Pb–Co$_3$O$_4$ composite inert anodes obtained at different heating temperatures[a]

Heating temperature/°C	Oxygen evolution overpotential η/V			Tafel formula and related parameters				
	400 A m^{-2}	500 A m^{-2}	600 A m^{-2}	a	b	α	β	i_0/A cm^{-2}
260	0.878	0.900	0.917	1.283	0.295	0.207	0.793	4.519×10^{-5}
280	0.857	0.882	0.906	1.360	0.378	0.161	0.839	2.004×10^{-4}
300	0.825	0.852	0.876	1.330	0.368	0.166	0.834	2.417×10^{-4}
320	0.813	0.833	0.851	1.158	0.249	0.245	0.755	2.262×10^{-5}
340	0.768	0.792	0.817	1.203	0.315	0.194	0.806	1.508×10^{-4}

[a] Where, η is the oxygen evolution overpotential. a and b are constants, i_0 is the exchange current density, α and β are transfer coefficient.[32–34]

best electrocatalytic activity, while it was very difficult to prepare the composite inert anodes because of the precipitation of molten lead from the graphite mould at a pressure of 65 MPa. Thus, the heating temperature was more appropriate to be controlled at 320 °C.

Anodic polarization curves of Pb–PbO$_2$, Pb–Co$_3$O$_4$, Pb–Co$_3$O$_4$–PbO$_2$ composite inert anodes obtained at the heating temperature of 320 °C in the zinc electrowinning simulated solution, were shown in Fig. 2. The kinetic parameters of Tafel linear fitting and oxygen evolution overpotentials of the composite inert anodes were shown in Table 2.

As shown in Fig. 2 and Table 2, at the current densities of 400, 500 and 600 A m^{-2}, the oxygen evolution potentials or overpotentials of Pb–Co$_3$O$_4$ composite inert anodes were lower than those of Pb–PbO$_2$ and Pb–Co$_3$O$_4$–PbO$_2$ composite inert anodes obtained at the heating temperature of 320 °C. It can be concluded that Co$_3$O$_4$ particles improve the electrocatalytic activity obviously better than PbO$_2$ particles in the zinc electrowinning simulation solution. The good electro-catalytic capability of Co$_3$O$_4$ may be the main reason for the decreasing of the oxygen overpotential.[35–39]

The value of (a) closely associated with the initial oxygen evolution overpotential, which is the oxygen evolution overpotential of composite anode at 1 A m^{-2}. The value of (b) is directly relative to the transfer coefficient, whose relationship was shown by equations ($b = 2.303RT/\alpha F$, $\alpha + \beta = 1$). According to compare with Tafel formula and related parameters, there is not obviously changing. It indicates that microcosmic electrochemical reaction is stable.[40]
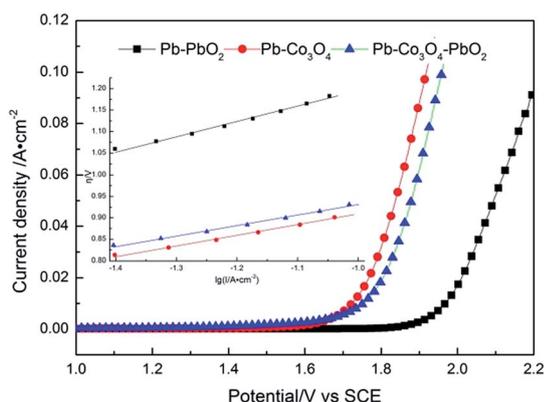
3.2 Cyclic voltammetry curves of the composite inert anodes

Cyclic voltammetry is one of the most simple and effective method of electrochemical test, which can control the change of electrode potential at a constant rate in the form of a triangular wave and measure one or more times for current of the electrode. Therefore, the redox reaction in the potential range of electrode can be observed and the limit and reversibility of electrode reaction can be determined.[41,42] The voltammetry charge $q*$ reflects the amounts of the surface active sites of the electrode, and it is an important parameter to evaluate the electrochemical active surface area.[43,44]

The cyclic voltammetry curves of Pb–Co$_3$O$_4$ composite inert anodes obtained at different heating temperatures were shown in Fig. 3, and its voltammetry charge $q*$ was exhibited in Table 3.

Fig. 2 Anodic polarization curves of Pb–PbO$_2$, Pb–Co$_3$O$_4$, Pb–Co$_3$O$_4$–PbO$_2$ composite inert anodes obtained at the heating temperature of 320 °C (scanning rate: $v = 5$ mV s^{-1}).

Table 2 The oxygen evolution kinetic parameters and overpotentials of Pb–PbO$_2$, Pb–Co$_3$O$_4$ and Pb–Co$_3$O$_4$–PbO$_2$ composite inert anodes obtained at the heating temperature of 320 °C

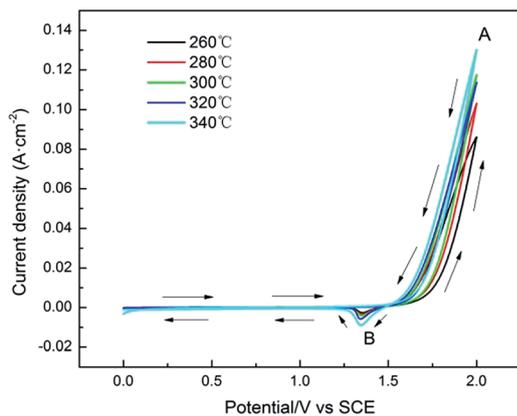| Anodes types	Oxygen evolution overpotential η/V			Tafel formula and related parameters				
	400 A m^{-2}	500 A m^{-2}	600 A m^{-2}	a	b	α	β	i_0/A cm^{-2}
Pb–PbO$_2$	1.062	1.086	1.112	1.553	0.358	0.170	0.830	4.592×10^{-5}
Pb–Co$_3$O$_4$	0.813	0.833	0.851	1.158	0.249	0.245	0.755	2.262×10^{-5}
Pb–Co$_3$O$_4$–PbO$_2$	0.838	0.858	0.876	1.262	0.308	0.198	0.802	7.951×10^{-5}

Fig. 3 Cyclic voltammetry curves of Pb–Co$_3$O$_4$ composite inert anodes obtained at different heating temperatures (scanning rate: $v = 50$ mV s^{-1}).

Table 3 Voltammetry charge $q*$ of Pb–Co$_3$O$_4$ composite inert anode obtained at different heating temperatures

Heating temperature/°C	Voltammetry charge, $q*$/C cm^{-2}
260	0.548
280	0.643
300	0.730
320	0.787
340	0.856

Fig. 4 Cyclic voltammetry curves Pb–PbO$_2$, Pb–Co$_3$O$_4$ and Pb–Co$_3$O$_4$–PbO$_2$ composite inert anodes obtained at the heating temperature of 320 °C (scanning rate: $v = 50$ mV s^{-1}).

Table 4 Voltammetry charge $q*$ of Pb–PbO$_2$, Pb–Co$_3$O$_4$ and Pb–Co$_3$O$_4$–PbO$_2$ composite inert anodes obtained at the heating temperature of 320 °C

Anode types	Voltammetry charge, $q*$/C cm^{-2}
Pb–PbO$_2$	0.325
Pb–Co$_3$O$_4$	0.787
Pb–Co$_3$O$_4$–PbO$_2$	0.530

As shown in Fig. 3, it was obvious that the redox reaction occurring on the surface of Pb–Co$_3$O$_4$ composite inert anodes was an irreversible. There were one oxidation peak A and one reduction peak B, in which peak A was produced by oxygen evolution reaction, and peak B was taken place by the reduction reaction of PbO$_2$ → Pb^{2+}. In addition, the peak values of oxidation peak A increased gradually with the rise of heating temperatures. It can be seen in Table 3 that the voltammetry charge $q*$ of Pb–Co$_3$O$_4$ composite inert anodes increased with the rise of heating temperatures, the main reason is that a part of lead powders were oxidized by residual air during the vacuum hot pressing process, and some lead dioxides were formed. According to the results in Fig. 3, the peak values of PbO$_2$ reduction peak B increased with the rise of heating temperatures, which reflects the increasing of the amounts of lead dioxides on the surface of the composite inert anodes, leading to the increasing of the surface active sites amounts and voltammetry charge $q*$.[45] Above research results display that the values of voltammetry charge $q*$ were increased with the raise of treated temperatures from 260 °C to 340 °C and the electrocatalytic activity of Pb–Co$_3$O$_4$ composite inert anodes were improved with increasing heating temperatures from 260 °C to 340 °C.

The cyclic voltammetry curves and voltammetry charge $q*$ of Pb–PbO$_2$, Pb–Co$_3$O$_4$ and Pb–Co$_3$O$_4$–PbO$_2$ composite inert anodes were shown in Fig. 4 and Table 4, respectively.

As shown in Fig. 4, there were also one oxidation peak A and one reduction peak B. The peak value of oxidation peak A of Pb–Co$_3$O$_4$ composite inert anode was the maximum, that of Pb–Co$_3$O$_4$–PbO$_2$ composite inert anode was in the middle and that of Pb–PbO$_2$ composite inert anode was the minimum. It can be seen in Table 4 that the voltammetry charge $q*$ of Pb–PbO$_2$, Pb–Co$_3$O$_4$, Pb–Co$_3$O$_4$–PbO$_2$ composite inert anodes were 0.787C cm^{-2}, 0.530C cm^{-2} and 0.325C cm^{-2}. To compare with doping level, the values of voltammetry charge $q*$ were increased obviously with doping Co$_3$O$_4$ particles than PbO$_2$ particles. Therefore, it can be concluded that the electrocatalytic activity of the composite inert anodes is related with particle types, the electrocatalytic activity of Pb–Co$_3$O$_4$ composite inert anode was higher than that of Pb–PbO$_2$ composite inert anode, displaying that Co$_3$O$_4$ particles improved the electrochemical performance obviously better than that of PbO$_2$ particles, this research result was consistent with that of Fig. 2 and Table 2.

3.3 Corrosion resistance of the composite inert anodes

Tafel polarization is a fast and effective technique to characterize the corrosion resistance of materials, which has been widely used in the field of the corrosion science.[46] The self-corrosion potential and the self-corrosion current density of the working electrode can be obtained. The value of self-corrosion potential (E_{corr}) expresses the self-corrosion ability

Fig. 5 Tafel polarization curves of Pb–Co₃O₄ composite inert anodes obtained at different heating temperatures (scanning rate: $v = 1$ mV s^{-1}).

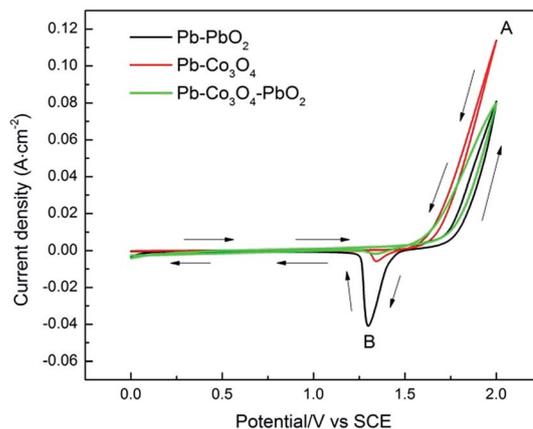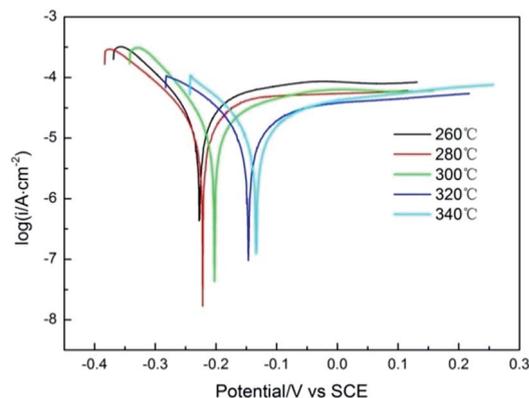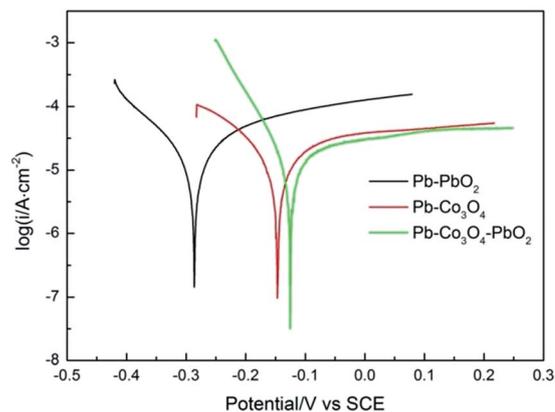**Fig. 6** Tafel polarization curves of Pb–PbO₂, Pb–Co₃O₄ and Pb–Co₃O₄–PbO₂ composite inert anodes obtained at the heating temperature of 320 °C (scanning rate: $v = 1$ mV s^{-1}).

of material without any external electric source, and the value of self-corrosion current density (i_{corr}) represents the corrosion rate of materials at the same potential.

The Tafel polarization curves of Pb–Co₃O₄ composite inert anodes obtained at different heating temperatures from 260 °C to 340 °C were shown in Fig. 5, E_{corr} and i_{corr} were shown in Table 5.

As shown in Fig. 5 and Table 5, the value of E_{corr} of Pb–Co₃O₄ composite inert anodes increased with the rise of the heating temperature from 260 °C to 340 °C and that of i_{corr} decreased with the rise of the heating temperatures, showing that the corrosion resistance of the composite inert anodes in the zinc electrowinning simulated electrolyte solution was enhanced with the rise of the heating temperatures. Pb–Co₃O₄ composite inert anode obtained at 340 °C possessed the highest E_{corr} (−0.134 V) and the lowest i_{corr} (2.305×10^{-5} A cm^{-2}), displaying that its corrosion resistance was best.

The Tafel polarization curves, E_{corr}, i_{corr} of Pb–PbO₂, Pb–Co₃O₄, Pb–Co₃O₄–PbO₂ composite inert anodes obtained at the heating temperature of 320 °C, were shown in Fig. 6 and Table 6. The E_{corr} value of Pb–Co₃O₄–PbO₂ composite inert anode was the highest (−0.125 V), and its i_{corr} value was the lowest (2.034×10^{-5} A cm^{-2}), displaying that the corrosion resistance of Pb–Co₃O₄–PbO₂ composite inert anodes obviously better than that of Pb–PbO₂ and Pb–Co₃O₄ composite inert

Table 6 Self-corrosion potential and self-corrosion current density of Pb–PbO₂, Pb–Co₃O₄ and Pb–Co₃O₄–PbO₂ composite inert anodes obtained at the heating temperature of 320 °C

Anode types	Self-corrosion potential E_{corr}/ V (vs. SCE)	Self-corrosion current density i_{corr}/A cm^{-2}
Pb–PbO₂	−0.286	7.298×10^{-5}
Pb–Co₃O₄	−0.146	5.461×10^{-5}
Pb–Co₃O₄–PbO₂	−0.125	2.034×10^{-5}

anodes in the zinc electrowinning simulated electrolyte solution.

The corrosion resistance the composite inert anodes is affected by particle property and of preparation process temperature. On the one hand, more lead powders were melted and recrystallized with the rise of heating temperatures, and then a more compact matrix was formed, in which it decreased the structure defects of Pb–Co₃O₄ composite inert anodes.[47–49] Therefore, the corrosion resistance of Pb–Co₃O₄ composite inert anodes was improved with increasing heating temperatures from 260 °C to 340 °C. On the other hand, PbO₂ and Co₃O₄ powders are insoluble particles in the zinc electrowinning simulated electrolyte solution, the simultaneous doping of Co₃O₄ and PbO₂ particles in the lead matrix improved the corrosion resistance more obviously than the individual doping of Co₃O₄ or PbO₂ particle. Thus, the corrosion resistance of Pb–Co₃O₄–PbO₂ composite inert anode was better than that Pb–PbO₂ or Pb–Co₃O₄ composite inert anode in the zinc electrowinning simulated electrolyte solution.

3.4 Electrochemical impedance spectroscopy of the composite inert anodes

In the case of electrochemical impedance spectroscopy (EIS) measurements, the working electrode potential was performed at 1.6 V potential chosen from the oxygen reaction controlled region over a frequency range of 100 kHz to 0.1 Hz with a signal

Table 5 Self-corrosion potential and self-corrosion current density of Pb–Co₃O₄ composite inert anodes obtained at different heating temperatures

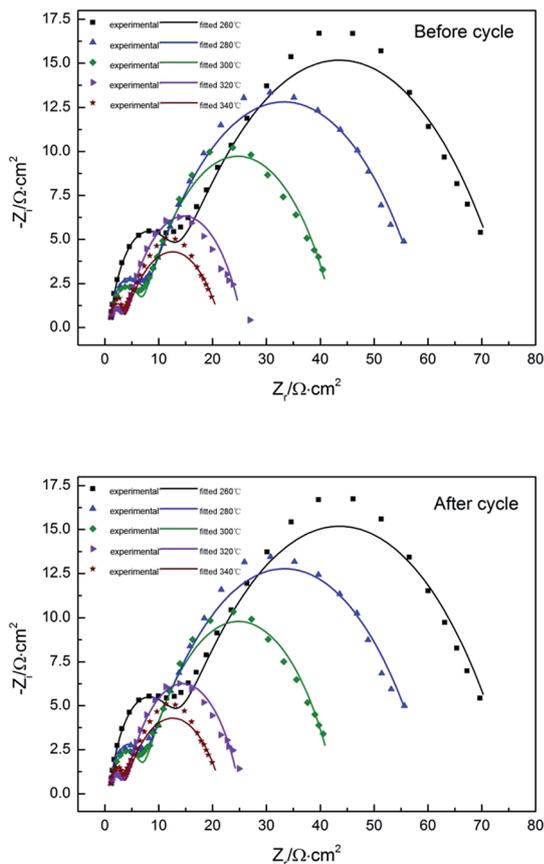| Heating temperature/°C	Self-corrosion potential E_{corr}/V (vs. SCE)	Self-corrosion current density i_{corr}/A cm^{-2}
260	−0.227	7.298×10^{-5}
280	−0.222	6.183×10^{-5}
300	−0.203	5.797×10^{-5}
320	−0.146	5.461×10^{-5}
340	−0.134	2.305×10^{-5}

Fig. 7 Nyquist plots before and after cycle of Pb–Co₃O₄ composite inert anodes obtained at different heating temperatures.
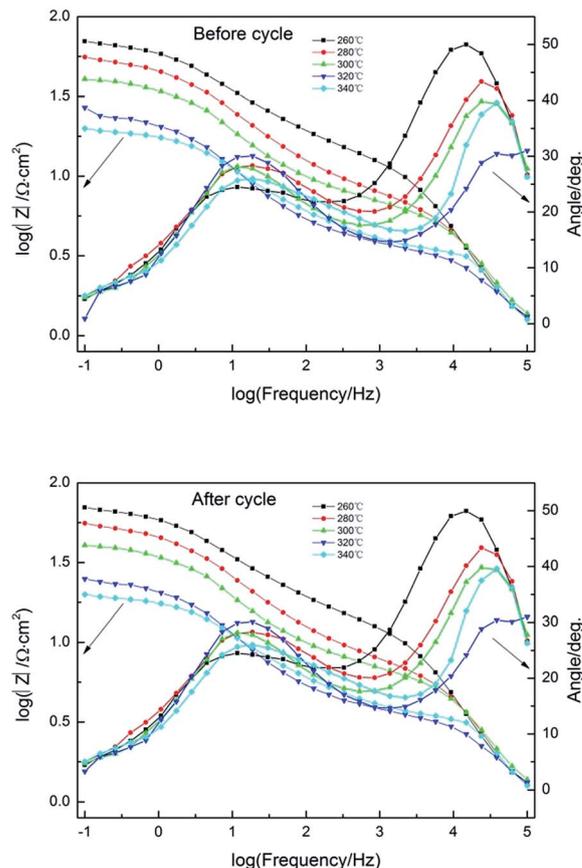

Fig. 9 Bode plots before and after cycle of Pb–Co₃O₄ composite inert anodes obtained at different heating temperatures.

amplitude perturbation of 10 mV.[40] Nyquist plots before and after cycle of Pb–Co₃O₄ composite inert anodes obtained at different heating temperatures were shown in Fig. 7, equivalent circuit of that was shown in Fig. 8, Bode plots before and after cycle of Pb–Co₃O₄ composite inert anodes were shown in Fig. 9 and EIS simulating parameters before and after cycle of equivalent circuit element of Pb–Co₃O₄ composite inert anodes were shown in Tables 7 and 8.

As shown in Fig. 7, the similar two profiles of the Nyquist plots reveal that the electrode oxygen evolution reaction mechanism does not change with the raise of heating temperatures. According to the calculation from Zsimp-win software, circuit $R(QR)(QR)$ was selected as equivalent circuit to simulate Nyquist plots. The values of Chi squared are close to 10^{-3} shown in Tables 7 and 8, which indicates the equivalent circuit can reflect oxygen evolution reaction more accurately on the surface of Pb–Co₃O₄ composite inert anodes. In present circuit, R_s is the
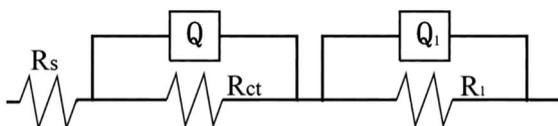

Fig. 8 Equivalent circuit of Pb–Co₃O₄ composite inert anodes obtained at different heating temperatures.

solution resistance and Q_1 is adsorption charge capacitance. R_1 and R_{ct} represent adsorption resistance and interfacial charge transfer resistance respectively. Q is corresponding to interfacial charge transfer. The values of R_s are all identical with each other, which show that the solutions have good conductivity. The charge transfer resistance R_{ct} can reflect difficulty of oxygen evolution reaction as an important parameter. The values of R_{ct} decreased with the raise of heating temperatures.[50] It reveals that the oxygen evolution reaction would be easy and the electro-catalytic capability can be improved by the raise of heating temperatures, this research result was consistent with analysis of anodic polarization curves and cyclic voltammetry curves. In addition, there are two peaks in Bode plots, and the number of peaks in the phase angle Bode plot equals the number of (CPE) elements in circuit.[51] It was consistent with analysis of Nyquist plots. To compare with the Nyquist and Bode plots before and after cycle of Pb–Co₃O₄ composite inert anodes, it shows that Pb–Co₃O₄ composite inert anodes have stable electrochemical performance.

Nyquist plots and Bode plots before and after cycle of Pb–PbO₂, Pb–Co₃O₄ and Pb–Co₃O₄–PbO₂ composite inert anodes obtained at the heating temperature of 320 °C were shown in Fig. 10, Tables 9 and 10 respectively. The circuit $R(QR)(QR)$ was selected as equivalent circuit due to values of Chi squared are

Table 7 EIS simulating before parameters of equivalent circuit element of Pb–Co$_3$O$_4$ composite inert anodes obtained at different heating temperatures

Heating temperature/°C	R_s/Ω cm^{-2}	Q/S cm^{-2} s^{-n}	n	R_{ct}/Ω cm^{-2}	Q_1/S cm^{-2} s^{-n}	n_1	R_1/Ω cm^{-2}	Chi squared
260	0.8178	2.747×10^{-5}	0.5586	64.57	2.178×10^{-5}	0.8535	10.640	9.620×10^{-4}
280	0.8678	3.305×10^{-3}	0.5662	53.78	1.417×10^{-5}	0.8783	5.505	9.894×10^{-4}
300	0.8747	3.802×10^{-3}	0.6233	36.48	2.566×10^{-5}	0.8142	5.619	1.426×10^{-3}
320	0.4866	5.591×10^{-3}	0.6640	21.97	1.094×10^{-4}	0.6789	3.229	1.845×10^{-3}
340	0.8685	7.662×10^{-3}	0.5541	18.44	3.211×10^{-6}	0.9944	2.460	5.998×10^{-3}

Table 8 EIS simulating after cycle parameters of equivalent circuit element of Pb–Co$_3$O$_4$ composite inert anodes obtained at different heating temperatures

Heating temperature/°C	R_s/Ω cm^{-2}	Q/S cm^{-2} s^{-n}	n	R_{ct}/Ω cm^{-2}	Q_1/S cm^{-2} s^{-n}	n_1	R_1/Ω cm^{-2}	Chi squared
260	0.8936	2.724×10^{-5}	0.5595	64.47	1.865×10^{-5}	0.8935	10.550	1.206×10^{-3}
280	0.8822	3.354×10^{-3}	0.5587	54.42	1.138×10^{-5}	0.8822	5.298	1.061×10^{-3}
300	0.8801	3.753×10^{-3}	0.6295	36.30	2.650×10^{-5}	0.8107	5.823	1.719×10^{-3}
320	0.4827	5.405×10^{-3}	0.6707	21.46	1.130×10^{-4}	0.6758	3.252	1.320×10^{-3}
340	0.8393	7.670×10^{-3}	0.5532	18.50	4.786×10^{-6}	0.9581	2.507	5.704×10^{-3}

close to 10^{-3} shown in Tables 9 and 10. As shown in Table 8, the R_{ct} value of Pb–Co$_3$O$_4$ and Pb–PbO$_2$ composite inert anode are the minimum and maximum respectively. It shows that the

Fig. 10 Nyquist plots before and after cycle of Pb–PbO$_2$, Pb–Co$_3$O$_4$ and Pb–Co$_3$O$_4$–PbO$_2$ composite inert anodes obtained at the heating temperature of 320 °C.

oxygen evolution reaction would be easy by the doping of Co$_3$O$_4$. The Co$_3$O$_4$ particles improved the electrochemical performance obviously better than that of PbO$_2$ particles, this research result was consistent with analysis of anodic polarization curves and cyclic voltammetry curves. There are also two peaks in Bode plots, which displays that analysis of Nyquist plots is correct (Fig. 11).
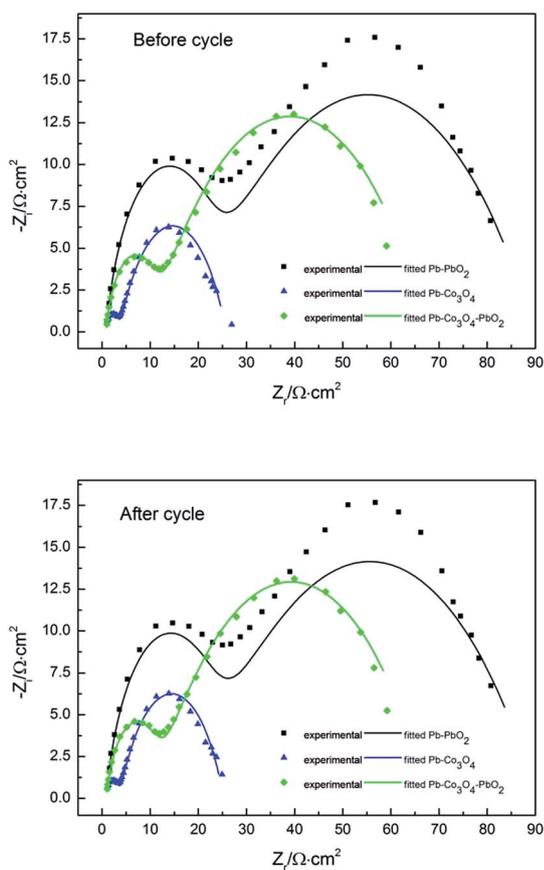
3.5 The phase structures and surface microstructures of the composite inert anodes

XRD patterns of Pb–PbO$_2$, Pb–Co$_3$O$_4$ and Pb–Co$_3$O$_4$–PbO$_2$ composite inert anodes obtained under the optimum preparation conditions, were shown in Fig. 12.

The surface microstructures of Pb, Co$_3$O$_4$ and PbO$_2$ powders were shown in Fig. 13, and those of Pb–PbO$_2$, Pb–Co$_3$O$_4$ and Pb–Co$_3$O$_4$–PbO$_2$ composite inert anodes were shown in Fig. 14.

The energy spectrum analysis of Pb–PbO$_2$ composite inert anode was shown in Fig. 15 and Table 11, that of Pb–Co$_3$O$_4$ composite inert anode was shown in Fig. 16 and Table 12, and that of Pb–Co$_3$O$_4$–PbO$_2$ composite inert anode was shown in Fig. 17 and Table 13.

As can be seen in Fig. 13, lead powders were irregular elliptical, Co$_3$O$_4$ particles were spherical, and PbO$_2$ particles were tetragonal. As shown in Fig. 14(a) and (c), 15, 17, Tables 11 and 13, it can be seen that a part of lead powers were melt to the recrystallized lead with compact microstructures during the vacuum hot pressing, and thereafter, some lead powders and recrystallized lead were also oxidized to PbO$_2$. Therefore, the characteristics of Pb and PbO$_2$ powder mixtures occurred in the microstructures of Pb–PbO$_2$ and Pb–Co$_3$O$_4$–PbO$_2$ composite inert anodes. As shown in Fig. 14(b) and (c), 16, 17, Tables 12 and 13, Co$_3$O$_4$ and PbO$_2$ particles were distributed uniformly in Pb–Co$_3$O$_4$ or Pb–Co$_3$O$_4$–PbO$_2$
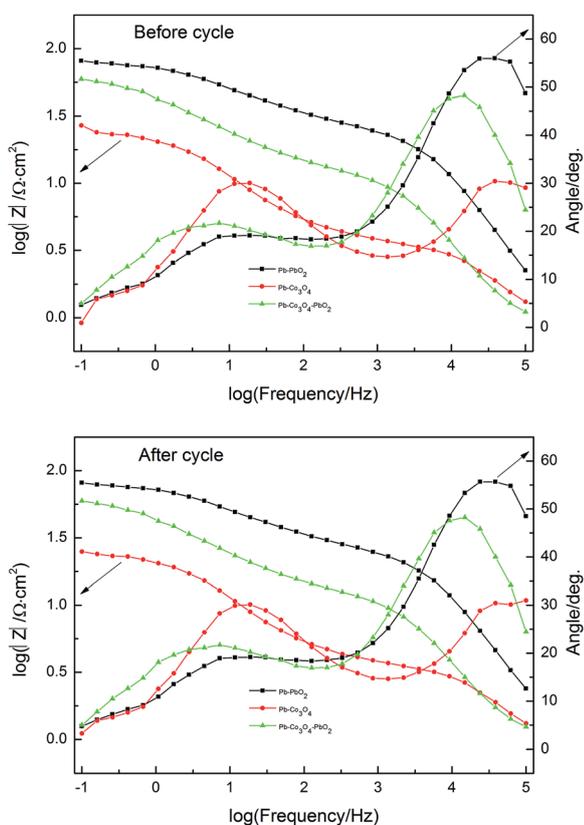
Table 9 EIS simulating parameters before cycle of equivalent circuit element of Pb–PbO$_2$, Pb–Co$_3$O$_4$ and Pb–Co$_3$O$_4$–PbO$_2$ composite inert anodes obtained at the heating temperature of 320 °C

Heating temperature/°C	R_s/Ω cm^{-2}	Q/S cm^{-2} s^{-n}	n	R_{ct}/Ω cm^{-2}	Q_1/S cm^{-2} s^{-n}	n_1	R_1/Ω cm^{-2}	Chi squared
Pb–PbO$_2$	0.6430	2.491 × 10^{-3}	0.4990	68.30	7.337 × 10^{-6}	0.8541	20.780	3.230 × 10^{-3}
Pb–Co$_3$O$_4$	0.4866	5.591 × 10^{-3}	0.6640	21.97	1.094 × 10^{-4}	0.6789	3.229	1.845 × 10^{-3}
Pb–Co$_3$O$_4$–PbO$_2$	0.7844	5.663 × 10^{-3}	0.5416	56.79	3.058 × 10^{-5}	0.8430	9.897	5.109 × 10^{-4}

Table 10 EIS simulating parameters after cycle of equivalent circuit element of Pb–PbO$_2$, Pb–Co$_3$O$_4$ and Pb–Co$_3$O$_4$–PbO$_2$ composite inert anodes obtained at the heating temperature of 320 °C

Heating temperature/°C	R_s/Ω cm^{-2}	Q/S cm^{-2} s^{-n}	n	R_{ct}/Ω cm^{-2}	Q_1/S cm^{-2} s^{-n}	n_1	R_1/Ω cm^{-2}	Chi squared
Pb–PbO$_2$	0.6560	2.534 × 10^{-3}	0.4972	68.42	8.095 × 10^{-6}	0.8431	21.080	3.587 × 10^{-3}
Pb–Co$_3$O$_4$	0.4827	5.405 × 10^{-3}	0.6707	21.46	1.130 × 10^{-4}	0.6758	3.252	1.320 × 10^{-3}
Pb–Co$_3$O$_4$–PbO$_2$	0.8150	3.942 × 10^{-3}	0.5475	56.31	3.942 × 10^{-5}	0.8132	10.370	6.854 × 10^{-4}

Fig. 11 Bode plots before and after cycle of Pb–PbO$_2$, Pb–Co$_3$O$_4$ and Pb–Co$_3$O$_4$–PbO$_2$ composite inert anodes obtained at the heating temperature of 320 °C.

3.6 The performance of current inert anodes compared with others

The performance of inert anodes compared with other related inert anodes in the literatures were show in Table 14.

There are five types of inert anodes in the table. The Pb–Co$_3$O$_4$ inert anodes were obtained by vacuum hot pressing technique in our research. The Al/Pb/α-PbO$_2$–WC inert anodes
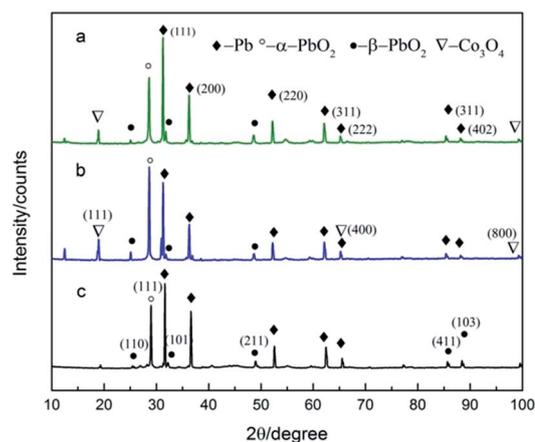
Fig. 12 XRD patterns of Pb–PbO$_2$, Pb–Co$_3$O$_4$ and Pb–Co$_3$O$_4$–PbO$_2$ composite inert anodes with (a) Pb–Co$_3$O$_4$–PbO$_2$, (b) Pb–Co$_3$O$_4$ and (c) Pb–PbO$_2$.
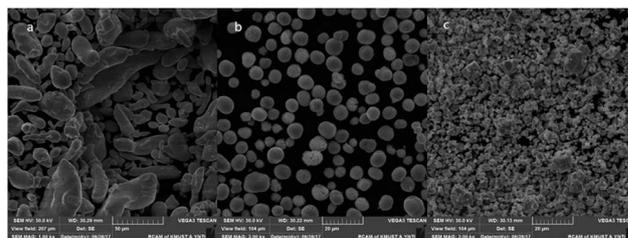
Fig. 13 Surface microstructures of with Pb (a), Co$_3$O$_4$ (b) and PbO$_2$ (c) powders.

composite inert anodes, which solved the problems of lower dispersion uniformity for the composite inert anodes prepared by composite electrodeposition or traditional casting technique. Above research results show that the morphologies and properties of Co$_3$O$_4$ and PbO$_2$ particles in the composite inert anodes were kept during the vacuum hot pressing.
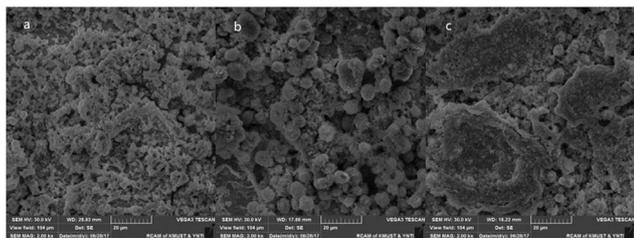
Fig. 14 Surface microstructures of Pb–PbO$_2$ (a), Pb–Co$_3$O$_4$ (b) and Pb–Co$_3$O$_4$–PbO$_2$ (c) composite inert anodes.
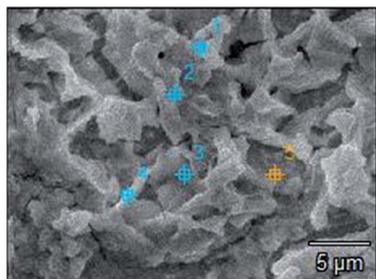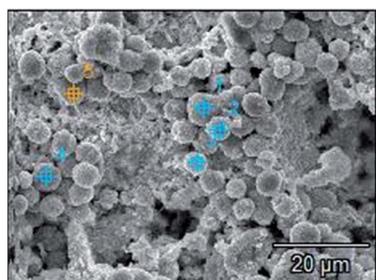

Fig. 15 The energy spectrum analysis of Pb–PbO$_2$ composite inert anode.

Table 11 The energy spectrum analysis of Pb–PbO$_2$ composite inert anode

Points	at% of O	at% of Pb	wt% of O	wt% of Pb
pt1	41.19	58.81	10.43	89.57
pt2	40.42	59.58	11.81	88.19
pt3	36.69	63.31	11.92	88.08
pt4	36.09	63.91	10.51	89.49
pt5	34.64	65.36	6.96	93.04

Fig. 16 The energy spectrum analysis of Pb–Co$_3$O$_4$ composite inert anode.
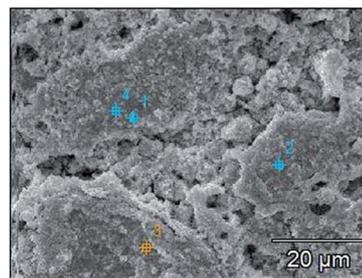

Fig. 17 The energy spectrum analysis of Pb–Co$_3$O$_4$–PbO$_2$ composite inert anode.

were studied by S. W. He *et al.*[7] The performance of Al/Pb–PANI–WC inert anodes was studied by R. D. Xu. *et al.*[52] The electrochemical properties of Pb-0.3% Ag/Pb–WC and Pb–1% Ag inert anodes were measured by S. He *et al.*[53] It can be seen from the table above that the oxygen evolution overpotential of Pb–Co$_3$O$_4$ inert anodes were obviously lower than other inert anodes. According to the experimental data of different types of inert anodes, the Pb–Co$_3$O$_4$ inert anodes showed better electrochemical performance than other inert anodes.

4. Conclusions

Pb–PbO$_2$, Pb–Co$_3$O$_4$ and Pb–Co$_3$O$_4$–PbO$_2$ composite inert anodes were prepared by vacuum hot pressing technique from the mixtures of lead powders, Co$_3$O$_4$ and PbO$_2$ particles in a fixed mould, and the uniform distributions of Co$_3$O$_4$ and PbO$_2$ particles in the composite inert anodes have been obtained.

Increasing heating temperatures from 260 °C to 340 °C was favourable to the reduction of oxygen evolution potentials or overpotentials of Pb–Co$_3$O$_4$ composite inert anodes. Co$_3$O$_4$ particles improved the electrocatalytic activity obviously better than PbO$_2$ particles in the zinc electrowinning simulated solution.

The corrosion resistance of Pb–Co$_3$O$_4$ composite inert anodes was enhanced with the rise of the heating temperatures from 260 °C to 340 °C. The simultaneous doping of Co$_3$O$_4$ and PbO$_2$ particles in the lead matrix improved the corrosion resistance more obviously than the individual doping of Co$_3$O$_4$ or PbO$_2$ particle.

The vacuum hot pressing technique solved the problem of lower dispersion uniformity for the composite inert anodes prepared by composite electrodeposition or traditional casting technique.

Table 12 The energy spectrum analysis of Pb–Co$_3$O$_4$ composite inert anode

Points	at% of O	at% of Co	at% of Pb	wt% of O	wt% of Co	wt% of Pb
pt1	59.71	21.53	18.76	25.51	34.46	40.03
pt2	37.07	20.82	42.11	5.62	11.64	82.74
pt3	18.50	8.50	73.00	3.58	6.07	90.35
pt4	36.69	57.75	5.56	11.41	66.19	22.40
pt5	30.60	6.24	63.16	5.18	4.11	90.71

Table 13   The energy spectrum analysis of Pb–Co$_3$O$_4$–PbO$_2$ composite inert anode by point scanning

Points	at% of O	at% of Co	at% of Pb	wt% of O	wt% of Co	wt% of Pb
pt1	26.46	14.70	58.84	4.23	8.82	86.95
pt2	24.79	33.10	42.09	5.95	17.99	76.06
pt3	34.21	27.91	37.88	9.94	17.76	72.30
pt4	31.41	34.02	34.57	10.25	22.77	66.98

Table 14   The performance of current inert anodes compared with other related inert anodes in the literature

Anode types	Oxygen evolution overpotential η/V			Self-corrosion potential E_{corr}/V (vs. SCE)	Self-corrosion current density i_{corr}/A cm^{-2}
	400 A m^{-2}	500 A m^{-2}	600 A m^{-2}		
Pb–Co$_3$O$_4$	0.813	0.833	0.851	−0.146	5.461×10^{-5}
Al/Pb/α-PbO$_2$–WC	0.807	0.839	0.866	1.186	9.045×10^{-6}
Al/Pb–PANI–WC	—	0.941	—	−0.470	4.506×10^{-3}
Pb-0.3% Ag/Pb–WC	—	0.926	0.940	−0.522	9.500×10^{-3}
Pb–1% Ag	—	1.171	1.182	−0.505	5.170×10^{-3}

Conflicts of interest

There are no conflicts to declare.

References

1 M. Bestetti, U. Ducati, G. H. Kelsall, G. Li and E. Guerra, Can. Metall. Q., 2013, 40, 451–458.
2 R. D. Xu, L. P. Huang, J. F. Zhou, P. Zhan, Y. Y. Guan and Y. Kong, Hydrometallurgy, 2012, 125, 8–15.
3 A. Felder and R. D. Prengaman, JOM, 2006, 58, 28–31.
4 H. T. Yang, H. R. Liu, Y. C. Zhang, B. M. Chen, Z. C. Guo and R. D. Xu, Int. J. Miner., Metall. Mater., 2013, 20, 986–993.
5 M. Petrova, Z. Noncheva, T. Dobrev, N. Kounchev, D. Petrov, V. Mihnev and D. Buttinelli, Hydrometallurgy, 1996, 40, 293–318.
6 R. H. Newnham, J. Appl. Electrochem., 1992, 22, 116–124.
7 S. W. He, R. D. Xu and G. Hu, RSC Adv., 2016, 6, 3362–3371.
8 Y. C. Zhang, B. M. Chen, H. T. Yang and Z. C. Guo, Trans. Nonferrous Met. Soc. China, 2014, 21, 83–88.
9 A. H. Ras and J. F. van Staden, J. Appl. Electrochem., 1999, 29, 313–319.
10 A. B. Velichenko, V. A. Knysh, T. V. Luk'yanenko, Y. A. Velichenko and D. Devilliers, Mater. Chem. Phys., 2012, 131, 686–693.
11 Y. Dan, H. Lu, X. Liu, H. Lin and J. Zhao, Int. J. Hydrogen Energy, 2011, 36, 1949–1954.
12 X. Li, X. Li, S. Tang, J. Yang, W. Li, B. Luo and S. Li, Appl. Surf. Sci., 2014, 311, 357–361.
13 N. E. Bagshaw, J. Power Sources, 1995, 53, 25–30.
14 R. D. Prengaman, J. Power Sources, 1997, 67, 267–278.
15 H. Okamoto, ASM International, 2000.
16 S. Venugopalan, J. Power Sources, 1994, 48, 371–384.
17 B. Panda, S. C. Das and R. K. Panda, Hydrometallurgy, 2009, 95, 87–91.
18 E. Rocca and J. Steinmetz, Electrochim. Acta, 1999, 44, 4611–4618.
19 D. Velayutham and M. Noel, J. Appl. Electrochem., 1993, 23, 922–926.
20 A. Hrussanova, L. Mirkova and T. Dobrev, Hydrometallurgy, 2001, 60, 199–213.
21 S. K. Meher and G. R. Rao, J. Phys. Chem. C, 2011, 115, 15646–15654.
22 Y. Liang, Y. Li, H. Wang, J. Zhou and J. Wang, Nat. Mater., 2011, 10, 780–786.
23 F. Tang, I. E. Anderson, T. Gnaupel-Herold and H. Prask, Mater. Sci. Eng. A, 2004, 383, 362–373.
24 D. L. McDanels, Metall. Trans. A, 1985, 16, 1105–1115.
25 R. J. Arsenault, L. Wang and C. R. Feng, Acta Metall. Mater., 1991, 39, 47–57.
26 Z. Tan, Z. Li, G. Fan, et al., Diam. Relat. Mater., 2013, 31, 1–5.
27 Z. Tan, Z. Li, G. Fan, et al., Compos. B Eng., 2013, 47, 173–180.
28 W. Shen, W. Shao, Q. Wang, et al., Fusion Eng. Des., 2010, 85, 2237–2240.
29 E. E. Abd El Aal, J. Power Sources, 1998, 75, 36–43.
30 V. Otieno-Alego, G. A. Hope, H. J. Flitt, G. A. Cash and D. P. Schweinsberg, Corros. Sci., 1992, 33, 1719–1734.
31 Y. Q. Lai, Y. Li, L. X. Jiang, W. Xu and X. J. Lv, J. Electroanal. Chem., 2012, 671, 16–23.
32 K. C. Neyerlin, W. Gu, J. Jorne and H. A. Gasteiger, J. Electrochem. Soc., 2007, 154, B631–B635.
33 J. Zhou, R. Xu and B. Chen, Adv. Sci. Lett., 2011, 4, 1225–1229.

34 I. Ivanov, Y. Stefanov, Z. Noncheva, M. Petrova and T. Dobrev, *Hydrometallurgy*, 2000, **57**, 125–139.

35 Z. Y. Li, P. T. Bui, D. H. Kwak, M. S. Akhtar and O. B. Yang, *Ceram. Int.*, 2016, **42**, 1879–1885.

36 X. Wang, X. Y. Chen, L. S. Gao, H. G. Zheng, Z. D. Zhang and Y. T. Qian, *J. Phys. Chem. B*, 2004, **108**, 16401–16404.

37 F. Wang, C. C. Lu, Y. F. Qin, C. C. Liang, M. S. Zhao, S. C. Yang, Z. B. Sun and X. P. Song, *J. Power Sources*, 2013, **235**, 67–73.

38 V. H. Nguyen and J. J. Shim, *Mater. Lett.*, 2015, **157**, 290–294.

39 X. W. Wang, M. X. Li, Z. Chang, Y. Q. Yang, Y. P. Wu and Z. Liu, *ACS Appl. Mater. Interfaces*, 2015, **7**, 2280–2285.

40 Q. Zhang and Y. Hua, *Acta Phys.–Chim. Sin.*, 2011, **27**, 149–155.

41 K. Polat, M. L. Aksu and A. T. Pekel, *J. Appl. Electrochem.*, 2002, **32**, 217–223.

42 R. Wartena, J. Winnick and P. H. Pfromm, *J. Appl. Electrochem.*, 2002, **32**, 415–424.

43 H. Vogt, *Electrochim. Acta*, 1994, **39**, 1981–1983.

44 K. W. Kim, E. H. Lee, J. S. Kim, K. H. Shin and K. H. Kim, *Electrochim. Acta*, 2002, **46**, 915–921.

45 M. Clancy, C. J. Bettles, A. Stuart and N. Birbilis, *Hydrometallurgy*, 2013, **131–132**, 144–157.

46 K. V. Subramaniam and M. Bi, *Corros. Sci.*, 2010, **52**, 2725–2735.

47 R. A. Johns and D. A. Blackburn, *Thin Solid Films*, 1975, **25**, 291–300.

48 G. F. Bolling and W. C. Winegard, *Acta Metall.*, 1958, **6**, 283–287.

49 J. H. P. Watson, *Phys. Rev. B: Condens. Matter Mater. Phys.*, 1970, **2**, 1282–1286.

50 S. R. Mellsop, A. Gardiner and A. T. Marshall, *Electrocatalysis*, 2014, **5**, 445–455.

51 J. Huang, Z. Li, B. Y. Liaw and J. Zhang, *J. Power Sources*, 2016, **309**, 82–98.

52 R. D. Xu, L. P. Huang, J. F. Zhou, P. Zhan and Y. Y. Guan, *Hydrometallurgy*, 2012, **125**, 8–15.

53 S. He, R. Xu, J. Wang, S. Han and B. Chen, *J. Wuhan Univ. Technol.*, 2016, **31**, 811–817.